ARTICLE   OPEN

Computational discovery of ultra-strong, stable, and lightweight refractory multi-principal element alloys. Part II: comprehensive ternary design and validation

Kate L. M. Elder [1✉], Joel Berry[1], Aurélien Perron [1], Brandon Bocklund[1], Jibril Shittu[1], Connor J. Rietema [1], Hunter B. Henderson[1], Scott K. McCall[1] and Joseph T. McKeown [1]

Here the discovery of refractory multi-principal element alloys (MPEAs) with high-temperature strength and stability is pursued within a constrained and application-relevant design space. A comprehensive approach is developed and applied to explore all 165 ternary systems in the Al-Ce-Fe-Hf-Mo-Nb-Ta-Ti-V-W-Zr family. A subset of ternary systems that contain large areas in composition–temperature space with high strength and robust BCC phase stability is found. Twelve sets of high-performing alloys are identified, each set optimized for one combination of phase constraint, optimization target, and temperature range. Preliminary mechanical tests support the viability of the method. This work highlights the importance of considering phase stability, exploring non-equiatomic regions of composition space, and applying application-relevant constraints. *Parts I* and *II* provide three down-selection techniques for identifying high-performing BCC refractory MPEAs, design guidelines, and many candidates predicted to have BCC phase stability and strengths 2–3 times higher than any reported to date.

INTRODUCTION

This publication is *Part II* in the series "*Computational discovery of ultra-strong, stable, and lightweight refractory multi-principal element alloys.*"

Multi-principal element alloys (MPEAs) consist of two or more principal elements[1] and may contain non-principal elements[2]. These are different from conventional alloys that typically have only one principal component and minute amounts of other components[3]. Since their discovery in 2004[4,5], MPEAs have emerged as an exciting class of materials with a wide design space[6] and the potential for improved material properties, such as high strength[7]. Particularly relevant for this study is the demonstrated high yield strength (YS) at 1000–1800 K of refractory MPEAs with a body-centered cubic (BCC) structure[8]. However, the full range of elemental combinations in the BCC refractory MPEA design space has been highly underexplored[1,9], especially in terms of non-equiatomic compositions.

Many of the well-studied MPEAs, e.g., the Cantor alloy equiatomic CoCrFeMnNi[5], are composed of mostly transition metal elements[4,5,10–12]. A 2017 review article on MPEAs[1] reported that 85% of the studied alloys consisted of mostly transition metals while only 7% consisted of mostly refractory elements. However, refractory metals have a high melting point and are therefore good candidates for high-temperature applications[13]. Among BCC refractory MPEAs that are most well-studied and/or strongest at 1000 °C are the equiatomic alloys MoNbTaVW[8,14], HfMoNbTaZr[15], and CrMoNbV[16]. At 1000 °C, these alloys have YS values of 0.84, 0.93, and 1.06 GPa, respectively, and specific yield strength (SYS) values of 0.070, 0.085, and 0.134 GPa cm^{3}g^{-1}, respectively. These equiatomic alloys may be taken as baselines for high-strength MPEAs and as reference points for theoretical models[17]. Note, however, that CrMoNbV suffers from apparent

intrusion of a brittle intermetallic phase in equilibrium for $T \lesssim 1200\,°C$.

While the high melting point of refractory metals can lead to improved high-temperature properties, production, and testing challenges are quite significant[1]. Considering, in addition, the vast design space available, it is important to have analytical tools to efficiently narrow the search space so that any alloys tested experimentally have already been predicted to be, e.g., both strong and stable.

This two-part series aims to elucidate general design rules and provide both quick and thorough computational down-selection procedures to discover BCC refractory MPEAs in the Al-Cr-Fe-Hf-Mo-Nb-Ta-Ti-V-W-Zr element family with high-temperature strength, phase stability, and density. In *Part I*, key factors in designing BCC refractory MPEAs that are both strong and have stable solid solution phases are outlined and exemplified. Two efficient and complementary but non-comprehensive down-selection procedures are proposed and applied, one based on analysis of only equiatomic alloys and one based on analysis of the entire composition space in terms of the Pareto optimal front in YS–density space. As in *Part I*, an N-element system from which alloys can be formed is written with dashes between elements, e.g., the ternary system Cr-Nb-W. Equiatomic alloys are written without compositional subscripts, e.g., CrNbW, and non-equiatomic alloys are written with compositional subscripts, e.g., $Cr_{20}Nb_{50}W_{30}$.

Predictions in *Part I* are based on the analytic YS model of Maresca and Curtin for BCC MPEAs[17] and the CALPHAD (CALculation of PHAse Diagrams) method for computing phase equilibria[18,19]. Alloys consisting of solely single- and dual-BCC phases were included in the study, and alloys with maximized SYS were also separately examined. It was found that ternary alloys generally perform as well as or better than alloys with more elements, Mo and Hf are prevalent in down-selected alloys, and

[1]Materials Science Division, Lawrence Livermore National Laboratory, Livermore, CA 94550, USA. ✉email: elder7@llnl.gov

the Hf-Mo-Ta(+), Hf-Mo-Nb(+), Cr-Mo, and Cr-Mo-Ti systems are promising candidates, with predicted YS and SYS values higher than refractory MPEAs reported to date[16,20] and BCC phase stability. The notation (+) indicates that the system can optionally be expanded to include an additional element. Alloys with two BCC solid solution phases were also identified as a potentially fruitful area of further study. The importance of incorporating BCC phase stability into the design process to fully account for the trend of opposition between strength and phase stability and of separately optimizing specific strength for weight-sensitive applications was made apparent in the work of *Part I*.

However, (S)YS maximizations in *Part I* were performed at single temperatures, independent of behavior at other temperatures. Rapid changes in YS and phase stability with temperature were shown to cause rapid changes in the list of top-performing alloys. This motivates a design procedure that targets specific temperature ranges to adequately balance the potentially significant property variations with temperature. Additional constraints and considerations related to manufacturability, safety margins, and high-temperature creep are also needed to design alloys that meet all the criteria for manufacturability and service.

In *Part II*, down-selected alloys are required to satisfy more stringent criteria in terms of consistent behavior over specific temperature ranges and margins of safety from undesired phase formation or loss of strength during manufacturing and service. To maintain tractability and allow a detailed assessment of the full search space, the focus is restricted to ternary alloys (all ternaries in the Al-Cr-Fe-Hf-Mo-Nb-Ta-Ti-V-W-Zr element family), which were found in *Part I* to be generally as high- or higher-performing than alloys with more elements. Extension to alloys with four or more elements is relatively straightforward.

Computational and experimental details are outlined in "Methods", and alloy down-selection procedures and results are presented in "Results". All down-selected alloys consist solely of one or two BCC solid solution phases. As discussed in *Part I*, non-BCC phases such as intermetallics are avoided as they are known to induce detrimental brittleness. Sets of top-performing alloys are identified for four combinations of phase constraint and optimization targets: metastable alloy YS, equilibrium alloy YS, metastable alloy SYS, and equilibrium alloy SYS. As in *Part I*, the labels of metastable and equilibrium reference treatment of dual-phase BCC alloys. All discussion of metastability is with respect to dual-BCC solid solution phases. Each optimization is performed over three different temperature ranges between 1200 and 1800 K. Preliminary experimental validation of selected top-

performing candidates via room-temperature hardness testing is also presented. Results indicate that the methodology and implementation can predict key experimental trends with the quantitative accuracy needed to identify high-performing candidates. Key *Part II* results are discussed in "Discussion" and compared with those of *Part I* to assess the strengths, weaknesses, and complementary attributes of the different down-selection procedures and to verify the robustness of the design principles proposed in this work.

RESULTS

Discovery of high-performing ternary alloys

Here we examine the composition space of all 165 ternary systems from the Al-Cr-Fe-Hf-Mo-Nb-Ta-Ti-V-W-Zr element family to identify candidate compositions that maintain both high YS or SYS and acceptable BCC phase stability in the temperature range 1200–1800 K. For each ternary system, the entire composition space is investigated such that the minimum composition of each element is 2%.

As a first step to narrow the search space, we initially consider the behavior of all 165 ternary systems only at 1300 and 1800 K. As an example, the YS and phase stability information for the ternary systems Cr-Ta-W and Cr-Nb-W at 1300 K are shown in Fig. 1a and b, respectively. The semi-transparent gray overlay indicates regions where the fraction of BCC phases is less than 100%. In regions outside of the gray overlay, there may be 1 or 2 BCC phases.

To pass the first down-selection, a system must have a maximum YS of at least 1 GPa at 1300 K (in areas where the BCC phase fraction is 100%) and have roughly 20% or more of the area in composition space containing 100% BCC phases at both 1300 and 1800 K. Any recommend alloy in a ternary system will be from the region of composition space containing 100% BCC phases. The requirement that 20% of the composition space consists solely of BCC phases is to ensure that only ternary systems that have large domains without predicted intermetallic phases pass the down-selection. As seen in Fig. 1a, though the maximum YS in the Cr-Ta-W system is well above 1 GPa in the center of the domain, it does not pass down-selection because the majority of its composition space is <100% BCC.

The ternary system Cr-Nb-W does pass this down-selection as there is a large domain consisting of 100% BCC phases, and the YS in this domain is larger than 1 GPa at multiple points in composition space. In total, 16 promising ternary systems are
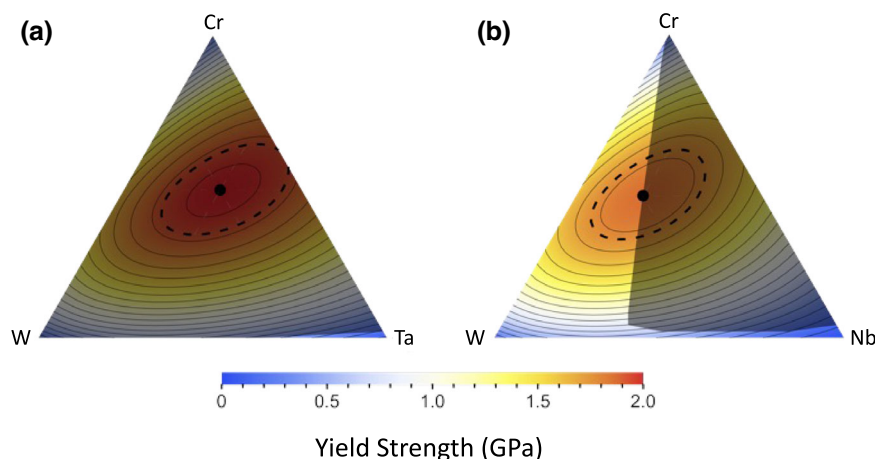

Fig. 1 Yield strength maps at 1300 K. Ternary yield strength maps in composition space for the ternary systems **a** Cr-Ta-W and **b** Cr-Nb-W at 1300 K. The black dot is the maximum YS in the system (Cr-Ta-W: 2.03 GPa, Cr-Nb-W: 1.87 GPa), the black dashed line is 0.1 GPa from the maximum, and the gray solid lines are 0.1 GPa increments. The semi-transparent gray overlay indicates regions with BCC phase fraction <100%.
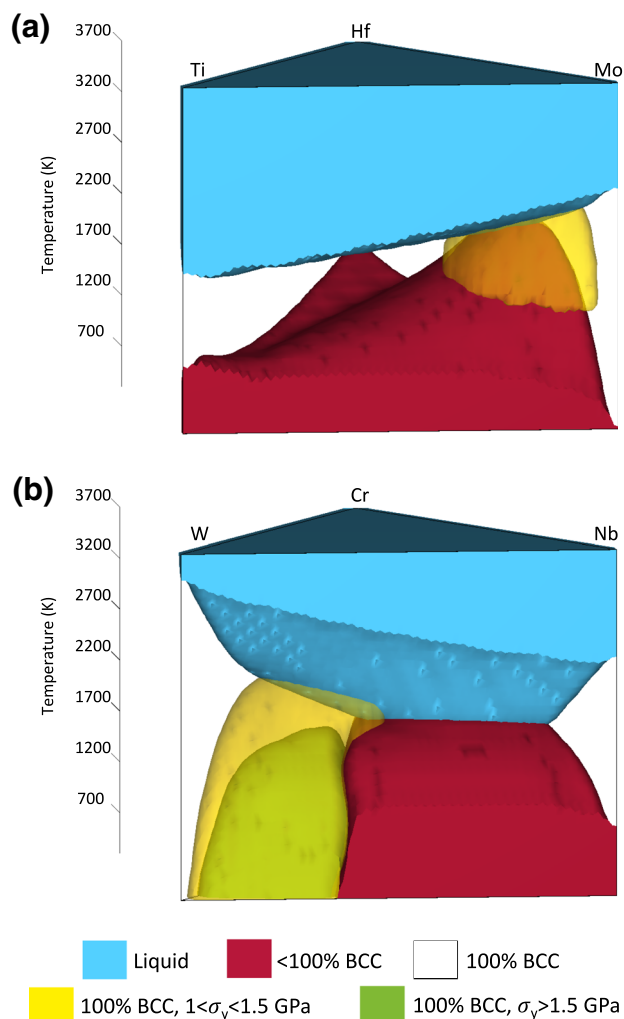
(a)

(b)

Fig. 2 3D yield strength maps. Yield strength and phase stability information plotted as a function of temperature over the composition space of the ternary systems **a** Hf-Mo-Ti and **b** Cr-Nb-W. Blue domains represent regions with liquid and red domains represent regions with <100% BCC phase fraction. In every other region, the BCC phase fraction is 100%. In yellow domains, $1 < \sigma_y < 1.5$ GPa, and in green domains, $\sigma_y > 1.5$ GPa.

identified in this first screening: Cr-Mo-Nb, Cr-Mo-Ti, Cr-Mo-V, Cr-Mo-W, Cr-Nb-W, Cr-Ti-W, Cr-V-W, Fe-Ti-W, Fe-V-W, Hf-Mo-Nb, Hf-Mo-Ta, Hf-Mo-Ti, Mo-Nb-Zr, Mo-Ta-Zr, Nb-W-Zr, and Ta-W-Zr.

For the next round of down-selection, the YS and phase stability are investigated over the temperature range 300–3700 K, in increments of 100 K, in addition to the composition space for each of the 16 ternary systems. Three-dimensional (3D) representations of this data for the ternary systems Hf-Mo-Ti and Cr-Nb-W are shown in Fig. 2a and b, respectively. Analogous 3D diagrams for the remaining 14 ternary systems are provided in Supplementary Figs. 1, 2, and 3, as discussed in Supplementary Note 1.

The blue domain contains any composition with a liquid phase fraction >0%, and the red domain contains any composition with a BCC phase fraction <100%. Everywhere else, the BCC phase fraction is 100%. The yellow and green domains are areas with high YS, between 1 and 1.5 GPa in the yellow domain and >1.5 GPa in the green domain. An optimal system would have minimal to no red domains, very large yellow and/or green domains, and a blue domain that appears only at very high temperatures. Throughout the composition spaces of the Cr-Mo-W, Cr-Mo-V, and Cr-V-W systems, the BCC phase fraction is always

100%, i.e., the red domain does not exist. The remaining systems were down-selected to minimize red domains while maximizing yellow and green ones.

Although candidate compositions are targeted for operation at 1200–1800 K, phase stability at lower temperatures is also considered. Depending on how the material is manufactured, other lower temperature phases (e.g., Laves phases) can become a concern. Systems where these phases appear at relatively low temperatures and in relatively low fractions are favored in the down-selection.

As shown in Fig. 2a, the composition–temperature space for Hf-Mo-Ti consists of a large irregularly shaped red domain that remains down to 300 K and a small yellow domain. The ternary system Hf-Mo-Ti was not included for further investigation due to its poor phase stability and small area with high YS. The ternary systems Fe-Ti-W and Ta-W-Zr were also removed as candidates for the same reason. The composition–temperature spaces of the remaining 13 ternary systems contain larger green and yellow domains that remain at lower temperatures. The ternary system Cr-Nb-W is shown in Fig. 2b as a representative example of a system flagged for further investigation. The Hf-Mo-Nb and Hf-Mo-Ta systems presented as marginal candidates because of the irregularly shaped non-BCC domains in their composition–temperature maps. However, their high performance predicted in *Part I* of the series motivated their inclusion in the final 13 systems here.

For each of the remaining 13 ternary systems, the composition space consisting solely of BCC phases was investigated to determine which alloy composition maximizes the YS and SYS across various temperature ranges. As in *Part I* of this series, within dual-BCC phase regions of the BCC-stable composition subspace, (S)YS is calculated for two approximate limiting cases. In the first case, the single-phase solid solution is assumed infinitely metastable with respect to phase separation. The term metastability is used in this work only with respect to BCC phase separation unless noted otherwise, as compositions with any non-BCC phases are excluded from consideration. In the second case, full phase separation to the equilibrium demixed compositions and volume fractions is assumed, and (S)YS is computed as an atomic phase fraction–weighted average of the (S)YS of the two equilibrium BCC phases. Throughout the text, calculations are distinguished by the treatment of dual-BCC phase regions. An example of the resulting difference between the two-phase stability constraints is shown for $Cr_{42}Mo_{26}W_{32}$ in Supplementary Fig. 4, as discussed in Supplementary Note 2.

As discussed in *Part I*, (S)YS results for metastable dual-phase alloys and single-phase alloys can be considered approximate upper bounds on (S)YS, as they assume the strongest state is maintained. They may nonetheless underpredict (S)YS in some cases due to limitations of the YS model and neglect of non-solid solution strengthening effects. (S)YS results for equilibrium dual-phase alloys involve greater uncertainty, with additional potential sources of underprediction and overprediction. Underpredictions may result from assuming full equilibration to the weakest of the possible states and neglecting strengthening contributions from phase interfaces[21], uneven load sharing between phases, and other non-solid solution strengthening effects. Overpredictions may result from assuming that initial plastic yielding occurs at the weighted average (S)YS of the two phases rather than at, e.g., the (S)YS of the weaker phase. Supplementary Figs. 5 and 6, as discussed in Supplementary Note 2 (along with Supplementary Fig. 4), provide examples of how the strengths of the demixed BCC phases differ and vary with temperature to exemplify the magnitude of potential variations in dual-phase (S)YS. This issue is also addressed further in the "*Part II* alloys" subsection of "Discussion".

In addition to the 100% BCC criterion, any recommended composition must be ≥4% from the phase boundary with any

regions that have <100% BCC phase fraction for all temperatures being considered. As BCC MPEAs retain their strength up to $0.6T_m$, where T_m is the melting temperature or liquidus[2], any candidate for a given operating temperature must satisfy $T \leq 0.6T_m$.

Under these constraints, the composition for each ternary system that maximizes the (S)YS across three temperature ranges (1200–1500 K, 1500–1800 K, 1200–1700 K) was determined. Results are provided in the "Yield strength" and "Specific yield strength" subsections. Generally, within a given ternary system, different compositions maximize the (S)YS at each temperature. Often, compositions that maximize the (S)YS ~1800 K do not have a stable BCC solid solution ~1200 K. Conversely, compositions that maximize the (S)YS ~1200 K often do not have a high enough melting temperature to operate ~1800 K. As a compromise between these effects, the different temperature ranges for the operation were investigated. Preliminary experimental validation of top-performing candidates is presented in the "Preliminary experimental validation" section.

When assuming metastability, if more than one composition in a given temperature range satisfies the BCC phase fraction and $0.6T_m$ criteria, the alloy composition is selected to maximize (S)YS at the highest temperature in the range. When assuming an equilibrium state, if more than one composition satisfies the criteria, two alloy compositions were selected; one to maximize the (S)YS at the highest temperature in the range and one to minimize dual-BCC regions.

The four different objective functions considered here (metastable YS, equilibrium YS, metastable SYS, equilibrium SYS) should ideally be optimized independently of each other. However, in the down-selection procedure used to identify the 16 then 13 ternary systems of interest, the YS was always calculated assuming solid solution metastability with respect to BCC phase separation, and SYS was not explicitly considered. Therefore, though the 13 selected systems have good overall metastable YS and BCC phase stability, they are not necessarily the best 13 systems in terms of equilibrium YS, metastable SYS, or equilibrium SYS. Thus some high-performing candidates may be missed for these latter three objectives. However, the 13 selected systems are likely to be among the best for these other three optimization targets, so we proceed with their maximization starting from these 13 ternaries.

Yield strength
Here the metastable and equilibrium compositions that maximize YS, subject to the constraints described in the "Discovery of high-performing ternary alloys" section, are reported for the 13 down-selected ternary systems across the three temperature ranges. Results are shown in Fig. 3. Solid and dashed lines are YS model predictions for single- and dual-phase BCC solid solutions, respectively, and square points connected by dotted lines are experimental data for MoNbTaVW (equilibrium)[17] and CrMoNbV (apparently metastable with respect to Laves phase)[16], for reference. The theory-predicted results for these alloys are also plotted, but only for $T \leq 0.6T_m$ for consistency.

For the equilibrium results (Fig. 3d–f, some ternary systems have two lines representing different compositions. In such cases, a primarily solid line indicates that the composition was selected to minimize dual-phase BCC regions, and a primarily dashed line indicates that the composition was selected to maximize overall YS. Compositions displayed with a combination of solid and dashed lines exhibit transitions between single- and dual-phase BCC equilibria, respectively, as temperature varies. Lines that do not span the entire temperature range reflect the $T \leq 0.6T_m$ criterion.

Metastable alloys—yield strength
The top-performing metastable candidates in terms of YS are represented in Fig. 3a–c. The YS always decreases as temperature

increases, as expected[22]. Over all three temperature ranges, the selected alloys all significantly outperform the theory-predicted and experimental data for MoNbTaVW and CrMoNbV (where available). Though (nearly) all selected alloys have two BCC phases in equilibrium at each temperature, the YS of the non-phase-separated state is reported, as indicated by the solid lines.

At 1200–1500 K (Fig. 3a), $Cr_{44}Nb_{16}W_{40}$ has the highest YS at each temperature, reaching a maximum of 1.96 GPa at 1200 K. Three of the recommended alloys ($Cr_{42}Mo_2W_{56}$, $Cr_{44}Ti_2W_{54}$, $Cr_{42}V_2W_{56}$) have only 2% of one element, the minimum required in this study. These are effectively Cr-W and Cr-Mo binaries, both of which have high equimolar strengths.

At 1500–1800 K (Fig. 3b), the selected compositions for each system are typically not the same as those selected for 1200–1500 K because of the higher temperatures and the $0.6T_m$ criterion. The relative YS rankings of the systems also typically change with temperature, e.g., $Nb_{30}W_{48}Zr_{22}$ has the highest YS from 1500 to 1800 K, reaching a maximum of 1.66 GPa at 1500 K. All candidates (except $Mo_{54}Nb_{28}Zr_{18}$, which only satisfies the $0.6T_m$ criterion to 1600 K) are W-rich, due to its high melting temperature. Three of the seven recommended alloys ($Cr_{42}Ti_6W_{52}$, $Cr_{34}Mo_2W_{64}$, $Cr_{42}V_2W_{56}$) are close to the Cr-W binaries.

At 1200–1700 K (Fig. 3c), $Cr_{40}Nb_{18}W_{42}$ (close to $Cr_{44}Nb_{16}W_{40}$ from the 1200–1500 K range) has the highest YS at each temperature, reaching a maximum of 1.96 GPa at 1200 K. Three of the nine recommended alloys ($Cr_{44}Ti_2W_{54}$, $Cr_{36}Mo_2W_{62}$, $Cr_{42}V_2W_{56}$) are effectively Cr-W binaries.

Equilibrium alloys—yield strength
The top-performing equilibrium candidates in terms of YS are represented in Fig. 3d–f. Over all three temperature ranges, every selected alloy outperforms the theory-predicted data for MoNbTaVW (CrMoNbV is not shown as it is not believed to be an equilibrium solid solution). For alloys that are single-phase BCC solid solutions at each temperature (solid lines), the YS decreases as temperature increases. However, for alloys in dual-BCC regions (dashed lines), the predicted YS typically increases with temperature. In such cases, the two equilibrium phases become more nearly equiatomic as temperature increases, increasing the solid solution strengthening effect. One of the BCC phases also has a lower YS than the other, and the fraction of the weaker phase tends to decrease as temperature increases, increasing the overall YS. Kinetic limitations may cause this type of YS to increase with temperature, if it indeed exists, to be difficult to observe experimentally.

At 1200–1500 K (Fig. 3d), single-phase $Hf_{22}Mo_{38}Ta_{40}$ has the highest YS between 1200 and 1400 K, reaching a maximum of 1.40 GPa at 1200 K, and dual-phase $Cr_{38}Mo_{46}Nb_{16}$ has the highest YS at 1500 K of 1.23 GPa. All four dual-phase alloys have solvus temperatures near 1500 K, which maximizes their 1200–1500 K YS. The top seven recommended single-phase alloys have a YS higher than the experimental data of MoNbTaVW at each temperature, while the others contain some YS values that fall between the experimental and theory-predicted data of MoNbTaVW. The YS model may similarly underpredict the strengths of these alloys. Seven of the 15 recommended alloys are effectively binary MPEAs, with <10% of one element, and one is a dilute ternary, with <10% of two elements.

The top candidates at 1500–1800 K (Fig. 3e) are significantly different but involve a similar mix of single- and dual-phase alloys. $Hf_{16}Mo_{52}Ta_{32}$ has the highest YS from 1500 to 1700 K, reaching a maximum of 1.32 GPa at 1500 K, while $Cr_{42}Ti_6W_{52}$ has the highest YS at 1800 K. $Cr_{38}Mo_{12}W_{50}$ changes from single to dual-phase near 1700 K, resulting in a change from increasing to decreasing YS. All nine recommended alloys have a higher YS than MoNbTaVW (experimental data and model predictions) at each temperature, except for $Cr_{30}V_2W_{68}$ at 1500 K. The six candidates that satisfy the $0.6T_m$ criterion over the entire temperature range are W-rich alloys. The dual-phase alloys have solvus temperatures near 1700
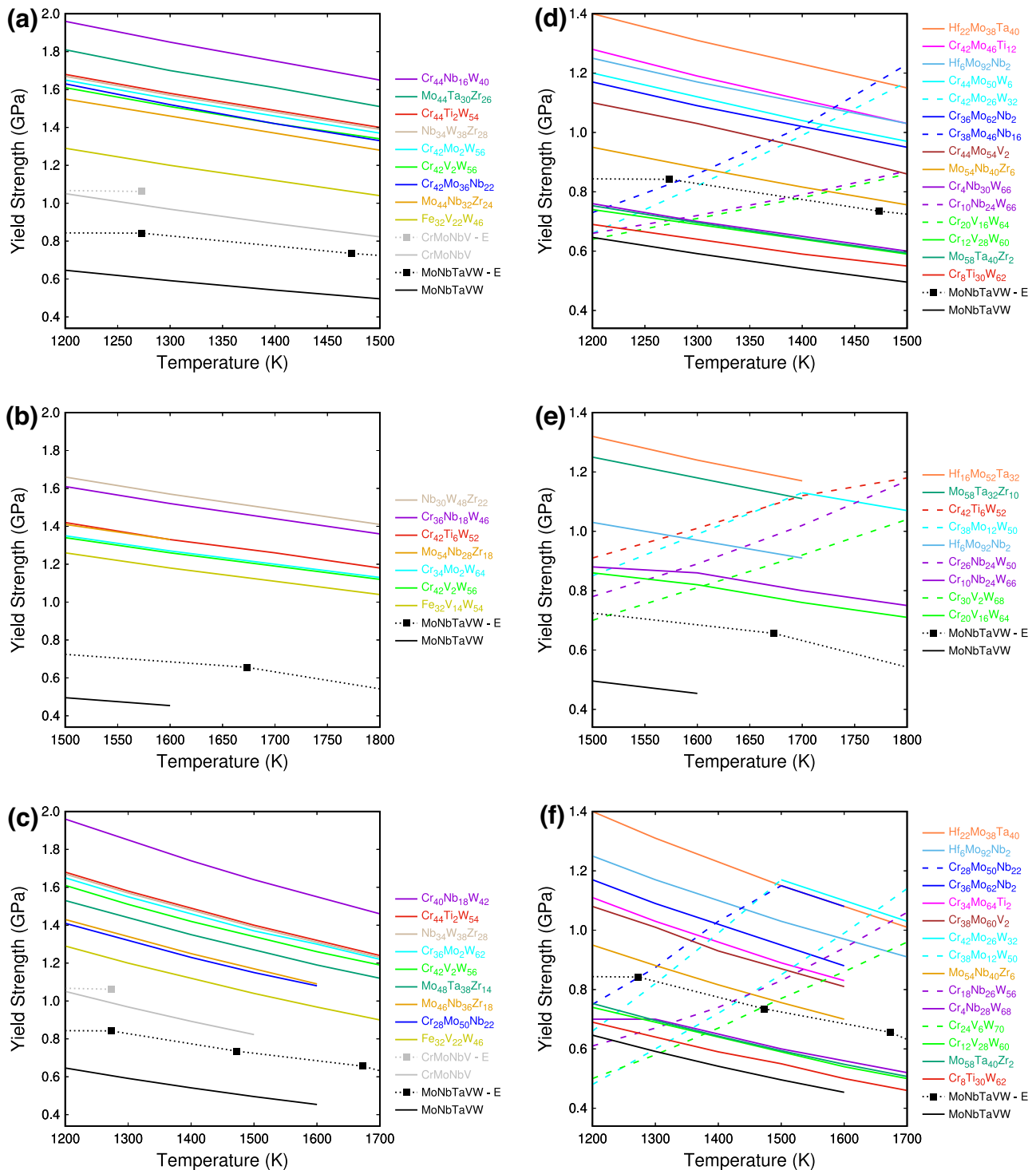
Fig. 3 Optimal alloys for high yield strength. Yield strength versus temperature for select ternary compositions that maximize YS **a–c** when metastable with respect to phase separation and **d–f** in phase equilibrium over three temperature ranges. Experimental (E) data for CrMoNbV[16] (metastable) and MoNbTaVW[8] (equilibrium) are included for reference. Solid and dashed lines in (**d–f**) are YS model predictions for single- and dual-phase BCC solid solutions, respectively.

or 1800 K, which maximizes their 1500–1800 K YS. Four of the 11 recommended alloys are effectively binary MPEAs, with ≤6% of one element, and one is a dilute ternary, with ≤6% of two elements.

A mix of single-, dual-, and combined single/dual-phase candidates is again observed over the 1200–1700 K range (Fig. 3f). As at 1200–1500 K, alloys from the ternary systems Hf-Mo-Ta, Hf-

Mo-Nb, Cr-Mo-Nb, Cr-Mo-W, and effective Cr-Mo binaries are top performers, though with somewhat changed compositions. Seven of the 10 alloys that satisfy the $0.6T_m$ criterion across the entire temperature range are W-rich, and two of the 10 alloys are Ta-rich (also high T_m). Some of the best performers among these are dual-phase or mixed single/dual-phase candidates, as these generally have higher atomic misfit and thus higher single-phase YS, with

adequate YS near the solvus temperature. Eight of the 15 recommended alloys are effectively binary MPEAs, with <10% of one element, and one is a dilute ternary, with <10% of two elements. A comparison between the recommended alloys under the metastable and equilibrium phase stability conditions is presented in Supplementary Note 3. For reference, the metastable and equilibrium alloys across the entire composition space of the 13 ternary systems that maximize YS at each temperature (as opposed to over finite temperature ranges) are presented in Supplementary Table 1, as discussed in Supplementary Note 4.

Specific yield strength
The metastable and equilibrium compositions that maximize SYS within the 13 down-selected ternary systems, subject to the constraints described in the introduction of the "Discovery of high-performing ternary alloys" section, are reported across the three temperature ranges in Fig. 4.

Metastable alloys—specific yield strength
The top-performing metastable candidates in terms of SYS are represented in Fig. 4a–c. As with metastable alloys for YS, each alloy's SYS decreases as temperature increases, and though (nearly) all selected alloys have two BCC phases in equilibrium at each temperature, the SYS of the non-phase-separated state is reported. Over all three temperature ranges, the selected alloys perform better than or similar to the theory-predicted and experimental SYS of CrMoNbV (where available) and significantly better than the equilibrium alloy MoNbTaVW. CrMoNbV thus appears to be a good metastable SYS candidate, though other alloys identified here may offer notably higher SYS and higher maximum operation temperatures.

At 1200–1500 K (Fig. 4a), $Cr_{42}Mo_{36}Nb_{22}$ has the highest SYS at each temperature, reaching a maximum of 0.189 GPa cm^{3}g^{-1} at 1200 K. Two of the eight recommended alloys ($Cr_{56}Ti_2W_{42}$, $Cr_{52}V_2W_{46}$) are effectively Cr-W binaries.

At 1500–1800 K (Fig. 4b), the selected compositions for each system are typically not the same as those selected for 1200–1500 K because of the higher temperatures and the $0.6T_m$ criterion. Whereas a Cr-Mo-Nb alloy has the highest SYS at 1200–1500 K, $Nb_{30}W_{46}Zr_{24}$ has the highest SYS from 1500 to 1800 K, reaching a maximum of 0.135 GPa cm^{3}g^{-1} at 1500 K. All six candidates are W-rich due to its high melting temperature, and one ($Cr_{46}V_2W_{52}$) is effectively a Cr-W binary.

At 1200–1700 K (Fig. 4c), $Mo_{46}Nb_{36}Zr_{18}$ and $Cr_{28}Nb_{50}W_{22}$ (similar to top performers in the 1200–1500 K range) have the best SYS up to 1600 K but do not satisfy the $0.6T_m$ criterion at 1700 K. $Cr_{40}Nb_{18}W_{42}$ and $Nb_{34}W_{38}Zr_{28}$ (similar to top performers in the 1500–1800 K range) are the highest SYS candidates that satisfy the $0.6T_m$ criterion over the entire range. Three of the nine recommended alloys ($Cr_{52}Ti_2W_{46}$, $Cr_{50}Mo_8W_{42}$, $Cr_{52}V_2W_{46}$) are nearly Cr-W binaries.

Equilibrium alloys—specific yield strength
The top-performing equilibrium candidates in terms of SYS are represented in Fig. 4d–f. Over all three temperature ranges, every selected alloy overall outperforms the theory-predicted data for MoNbTaVW, and most outperform the experimental data for MoNbTaVW (CrMoNbV is again not shown as it is not believed to be an equilibrium solid solution where data exists). As with the equilibrium YS candidates, the SYS can increase as temperature increases in dual-BCC regions as the two phases become more equiatomic and the phase fraction of the weaker phase decreases.

At 1200–1500 K (Fig. 4d), single-phase $Cr_{40}Mo_{48}Ti_{12}$ has the highest YS between 1200 and 1400 K, reaching a maximum of 0.153 GPa cm^{3}g^{-1} at 1200 K, and dual-phase $Cr_{44}Mo_{44}Nb_{12}$ has the highest YS at 1500 K of 0.144 GPa cm^{3}g^{-1}. The next four top

candidates are single-phase alloys, three are effectively Cr-Mo binaries, and one is nearly a Mo-Nb binary.

The top candidates at 1500–1800 K (Fig. 4e) are significantly different and include more dual-phase alloys. Single-phase $Hf_6Mo_{90}Nb_4$ is best from 1500 to 1700 K but does not reach 1800 K. Mixed-phase $Cr_{38}Ti_{12}W_{50}$ is best among alloys that span the entire temperature range, followed by three other Cr- and W-rich dual or mixed-phase alloys.

Another mix of single-, dual-, and combined single/dual-phase candidates is observed over the 1200–1700 K range (Fig. 4f). As at 1200–1500 K, top performers are dual/mixed-phase CrMoNb, single-phase CrMoTi, and effective CrMo binaries, though with somewhat changed compositions. However, these alloys reach only to 1600 K. Single-phase alloys from the Hf-Mo-Ta and Hf-Mo-Nb systems are top performers that satisfy the $0.6T_m$ criterion across the entire temperature range. The additional five alloys that satisfy the $0.6T_m$ criterion across the entire temperature range are the five weakest candidates. These are all dual- or mixed-phase Cr- and W-rich alloys except for the Ta-rich Mo-Ta-Zr candidate. These alloys are poorer SYS performers than their YS maximizing counterparts due to the high densities associated with W and Ta. However, as with the other temperature ranges, significant SYS margins over MoNbTaVW are predicted. Six of the 12 recommended alloys are effectively binary MPEAs, with ≤6% of one element, and two are effectively dilute ternaries, with ≤6% of two elements. A comparison between the recommended alloys under the metastable and equilibrium phase stability conditions is presented in Supplementary Note 3. For reference, the metastable and equilibrium alloys across the entire composition space of the 13 ternary systems that maximize SYS at each temperature (as opposed to over finite temperature ranges) are presented in Supplementary Table 2, as discussed in Supplementary Note 4.

Preliminary experimental validation
As an initial assessment of our computational results, 10 down-selected alloys from the "Discovery of high-performing ternary alloys" section were synthesized and subjected to room-temperature Vickers hardness testing as a surrogate for YS measurement. Hardness results and their conversion to YS are shown in Fig. 5. Nine alloys are ternaries containing little or no W, and one is $Cr_{37}Mo_{63}$, which was included to represent the several nearly binary high-performing Cr-Mo alloys. In this preliminary experimental validation, alloys with a high composition of W were excluded due to the difficulties of machining alloys with W because of their high melting point. As described in "Methods", the alloys were hardness tested at test scales of HV1 (1 kg load) and HV2 (2 kg load). None of the alloys cracked under the 1 kg load. One of the alloys ($Cr_{42}Mo_{46}Ti_{12}$) cracked under the 2 kg load. This suggested these alloys may have acceptable room-temperature ductility. In addition to this experimental testing, several binary, ternary, and quaternary alloys from the Cr-Mo-Nb-V family (and MoNbTaVW) were hardness tested at room temperature and compared with model predictions to further validate this study. This information is presented in Supplementary Fig. 7, as discussed in Supplementary Note 5.

The YS predicted assuming single-phase BCC metastability is also plotted in Fig. 5. The metastable predictions are taken as the most relevant measure since all of these alloys in the as-cast state have a moderate to high probability of maintaining a metastable single-phase BCC solid solution upon solidification and cooling, with some microsegregation expected. This is inferred from the CALPHAD-generated property diagrams (equilibrium phases and phase fractions versus temperature) presented in Supplementary Figs. 8 and 9, discussed in Supplementary Note 6. Each alloy is predicted to solidify as single-phase BCC somewhere between 2800 and 2000 K and then phase-separate into two BCC phases somewhere between 1600 and 1100 K. The exception is
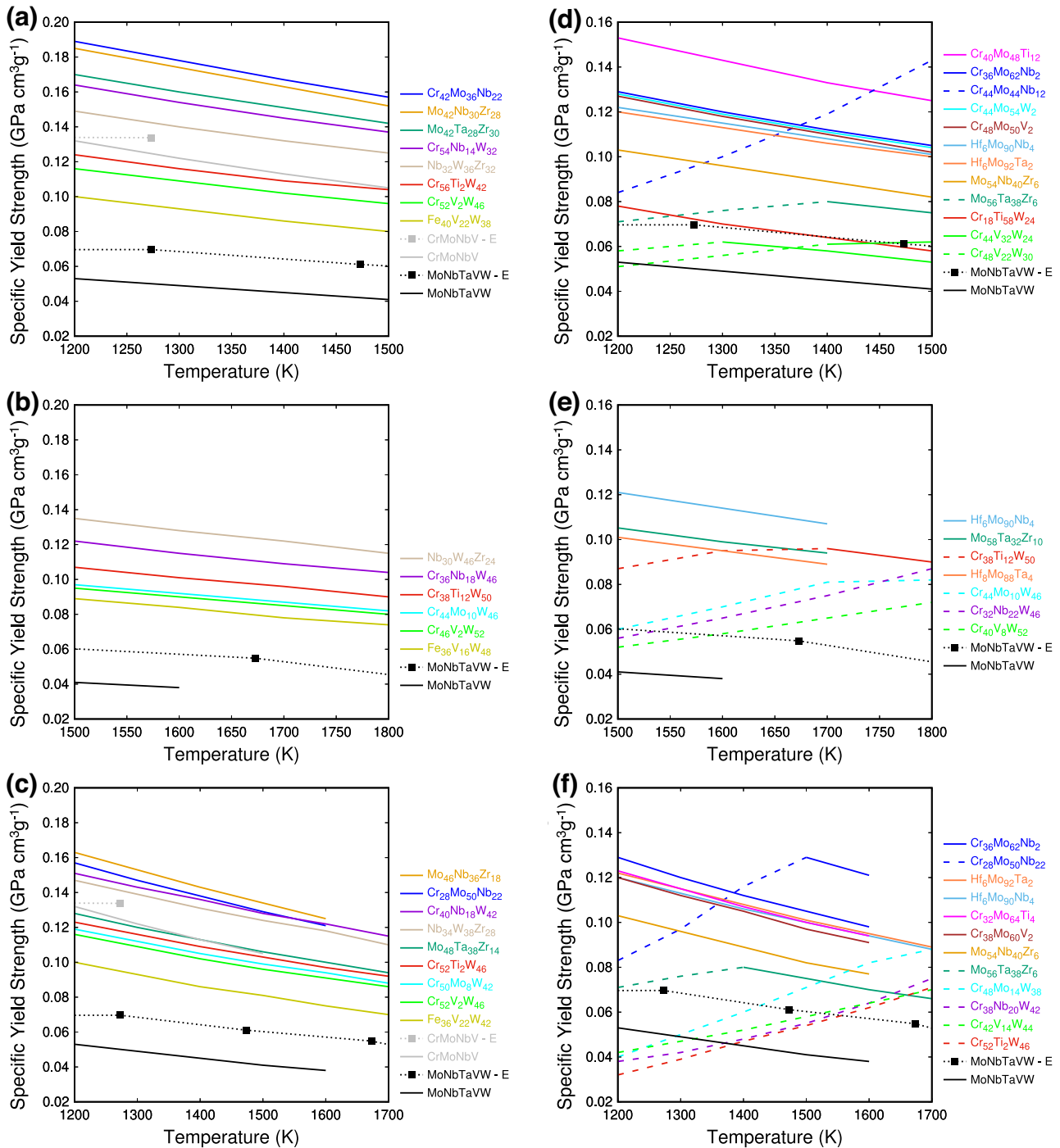
Fig. 4 **Optimal alloys for high specific yield strength.** Specific yield strength versus temperature for select ternary compositions that maximize SYS **a–c** when metastable with respect to phase separation and **d–f** in phase equilibrium over three temperature ranges. Experimental (E) data for CrMoNbV[16] (metastable) and MoNbTaVW[8] (equilibrium) are included for reference. Solid and dashed lines in (**d–f**) are YS model predictions for single- and dual-phase BCC solid solutions, respectively.

$Mo_{58}Ta_{40}Zr_2$, which is not predicted to phase-separate at all. Non-BCC phases (μ, C15, HCP) then appear between 1400 and 300 K in seven of the alloys, but their probability of formation upon solidification and cooling is judged relatively low given the slower nucleation and growth kinetics expected in this temperature range.

Eight of the 10 predictions are within 7–17% of the measured values. This is quite a good overall agreement, given that the YS model is expected to be less accurate at lower temperatures and

that the relation between YS and hardness is approximate. There is a consistent trend of moderate overprediction in that the predicted YS is higher than the experimental YS for all alloys except $Mo_{58}Ta_{40}Zr_2$. The two poorest predictions are for $Mo_{46}Nb_{36}Zr_{18}$ (46% over) and $Mo_{58}Ta_{32}Zr_{10}$ (27% over).

One possible cause of the observed overpredictions is microsegregation. As with phase separation, but to a lesser degree, the segregated regions will generally have lower predicted YS than the unsegregated nominal composition. Non-BCC phases could
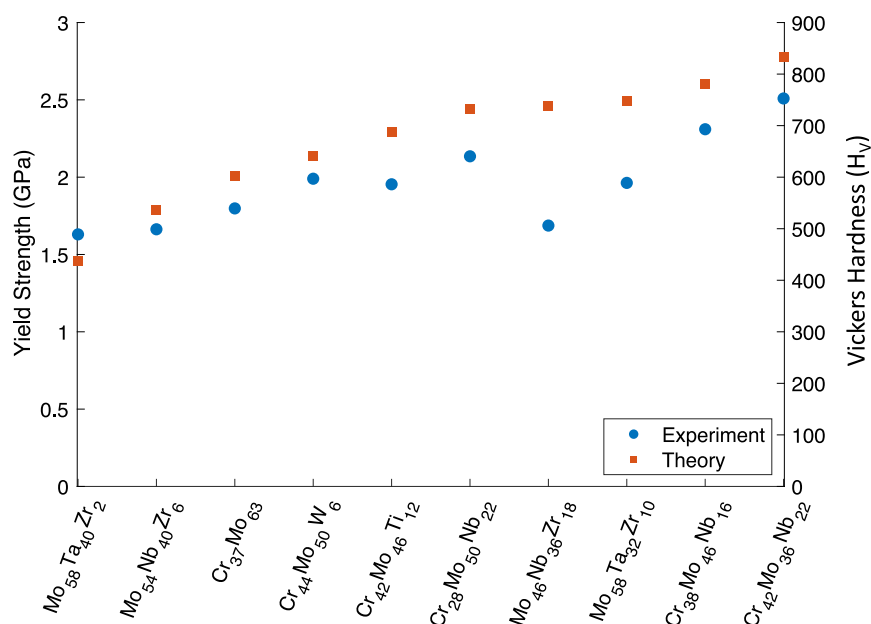
Fig. 5 Experimental comparison. Yield strength of a selection of top-performing alloys at room temperature obtained from converting the experimentally obtained Vickers hardness to YS (Experiment) and the predicted room-temperature YS assuming solid solution metastability with respect to all other phases (Theory). Vickers hardness is indicated on the right axis.

cause overprediction or underprediction, but, as noted, their probability of formation is relatively low, and we thus assume they are absent unless direct evidence is available. To assess these factors further, four alloys were selected for closer study: $Cr_{42}Mo_{36}Nb_{22}$ (the strongest alloy, 11% overpredicted), $Cr_{42}Mo_{46}Ti_{12}$ (an overall high-performing candidate, 17% overpredicted), $Mo_{46}Nb_{36}Zr_{18}$ (the poorest prediction, 46% overpredicted), and $Mo_{58}Ta_{40}Zr_2$ (the only underprediction, 11% underpredicted).

Energy dispersive spectroscopy (EDS) was used to quantify the distribution of elements for a representative area of the select four alloys. This information can be used to assess microsegregation and identify signs of non-solid solution phases. We note that uncertainties in the measured compositional fractions at the single pixel level are significant, i.e., the measurements are semi-quantitative. The results are intended to be illustrative of general effects and trends. Figure 6 shows the composition of each element in a representative area of $Cr_{42}Mo_{36}Nb_{22}$, along with a backscattered electron (BSE) SEM image for overall contrast. The corresponding images for the other three alloys are shown in Supplementary Figs. 10, 11, and 12, as discussed in Supplementary Note 7. The $Cr_{42}Mo_{36}Nb_{22}$ sample in Fig. 6 appears to be single-phase with microsegregation associated with a dendritic solidification structure. Signs of the phase separation predicted to initiate ~1500 K and the μ phase predicted to appear ~650 K (Supplementary Fig. 8b) are absent.

The composition maps are used to generate a predicted YS map for each alloy, assuming a single BCC solid solution at each pixel, as shown in Fig. 6a. The predicted YS varies significantly, from lower in the Mo-rich dendritic regions to higher in the Cr- and Nb-rich interdendritic regions. This heterogeneity from microsegregation, similar to phase separation, may account for a significant part of the modest theoretical overprediction for this alloy.

Figure 7 shows the predicted YS map for each of the four alloys, scaled to the maximum and minimum YS of the overall set. The red pixels in (b) and (d) are regions erroneously rich in Ti and Zr, respectively, which have been left out of the YS prediction, as discussed in Supplementary Note 7. $Cr_{42}Mo_{46}Ti_{12}$, like $Cr_{42}Mo_{36}Nb_{22}$, appears to be single-phase with a microsegregated dendritic solidification structure. Signs of the phase separation

predicted to initiate ~1200 K and the C15 Laves phase predicted to appear ~1100 K (Supplementary Fig. 8e) are absent. Heterogeneity from microsegregation may also account for a significant part of the modest theoretical overprediction for this alloy.

$Mo_{46}Nb_{36}Zr_{18}$ (Fig. 7c) exhibits a microsegregated dendritic solidification structure with a Zr-rich interdendritic phase. This may be the 100% Zr HCP phase predicted to appear ~1000 K (Supplementary Fig. 9a). The combined effects of microsegregation and strong Zr sequestering into a secondary phase thus seem to account for the larger deviation between experiment and theory for this alloy.

$Mo_{58}Ta_{32}Zr_2$ (Fig. 7d) is expected to be the most stable single-phase solid solution with the least microsegregation of the ten (see Supplementary Fig. 9d). It does appear to be largely single-phase with no clear microsegregation, though micron-scale zirconium oxide inclusions are visible. Neglecting these inclusions, it is thus reasonable that the YS prediction for $Mo_{58}Ta_{32}Zr_2$ is among the most accurate and is the only prediction below the experimental YS, given unaccounted-for strengthening contributions at room temperature (e.g., screw dislocations).

While the converted room-temperature hardness data shows good agreement with the predicted YS, especially after accounting for microsegregation and secondary phases, high-temperature testing is ultimately needed to fully assess the predictions made in this work. Nonetheless, this preliminary experimental comparison demonstrates that the YS and CALPHAD models capture the key relative trends and that the down-selection procedure identifies very hard alloys (with converted room-temperature YS between 1.6 and 2.5 GPa) with generally good solid solution metastability down to room temperature.

DISCUSSION

Trends in the preceding results are now examined, and key considerations in their interpretation are discussed. This is followed by a comparison of the current results with those of *Part I*.
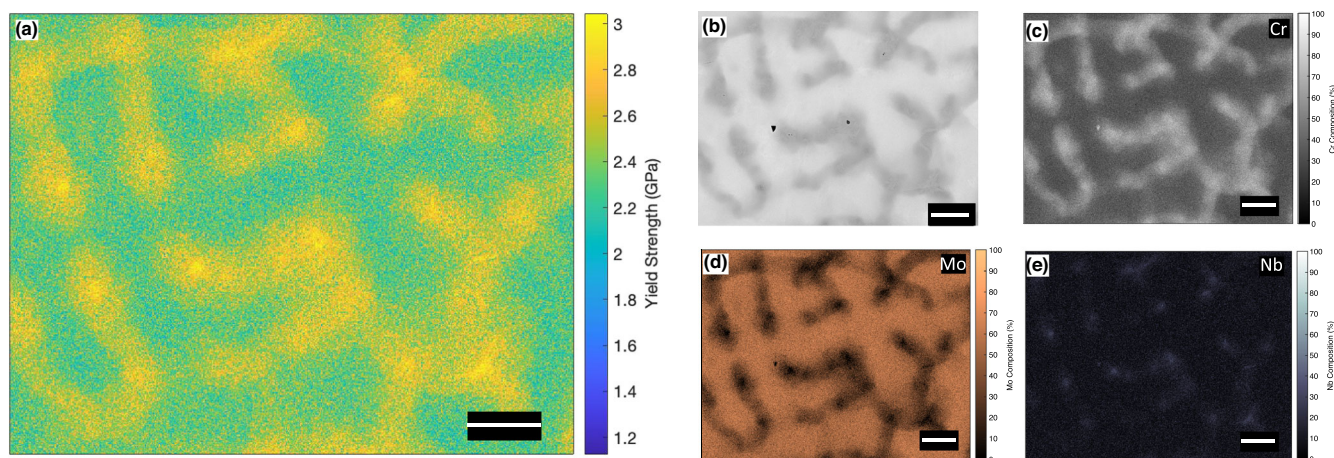
Fig. 6 EDS and YS information for Cr₄₂Mo₃₆Nb₂₂. EDS results and computed YS map for $Cr_{42}Mo_{36}Nb_{22}$. **a** Predicted YS map, **b** SEM backscattered electron image, and **c** Cr, **d** Mo, **e** Nb composition maps. Scale bar: 20 μm.

Part II alloys

The present results clearly demonstrate, as was observed in *Part I*, that phase stability constraints dramatically limit realizable strengths. At 1300 K, only 16 of the 165 ternary systems have a composition with a predicted YS above 1 GPa (in a region with 100% BCC phase stability) and a large area in composition space (≳20%) that is 100% BCC in equilibrium. The Cr-W-Zr system, for example, has compositions with predicted solid solution YS values >4 GPa at 1300 K but has no compositions that are 100% BCC in equilibrium.

The two different phase stability conditions employed, metastability and equilibrium, produce quite different sets of down-selected alloys. Of course, the metastable candidates require that a metastable solid solution can be stabilized with respect to phase separation inside any miscibility gaps. Through rapid cooling, it has been demonstrated that metastable phases can be stabilized in MPEAs[23] (also see "Preliminary experimental results" section). The lifetime of a metastable solid solution decreases as temperature increases, such that viable operation times become increasingly limited in the 1200–1800 K range. Thus the metastable predictions inside miscibility gaps should be considered upper bounds, dependent on target temperatures and exposure times for operation.

The top equilibrium candidates overall have lower (S)YS than the metastable candidates because the two demixed BCC solid solutions within miscibility gaps are virtually always weaker than the parent solid solution phase. The (S)YS difference is small near the solvus temperature but increases, often considerably, as temperature decreases. As discussed in *Part I*, in the "Discovery of high-performing ternary alloys" section of "Results", and in the "Strengths of recommended dual-BCC phase equilibrium alloys" subsection of Supplementary Information, more uncertainties are inherent in the predicted strengths of the equilibrium dual-BCC phase alloys. We thus recommend these alloys provisionally, reliant on further investigation.

The top two metastable and equilibrium candidates for YS and SYS from each of the three temperature ranges are listed in Table 1 for reference. Nine ternary systems and one binary system are represented, with 16 distinct alloys after accounting for duplicates and near duplicates (alloys within 5% of each other in 3D composition space).

Some of the 13 ternary systems studied in detail contain few or no alloys that satisfy our criteria at each temperature in a given range, especially in the 1500–1800 K and 1200–1700 K ranges. The $0.6T_m$ criterion is implicated at the high end, and the effect of phase separation and/or non-BCC phases is implicated at the low end. Cr-Mo-Nb, for example, has no compositions that are 100% BCC at every temperature with $0.6T_m \geq 1800$ K.

It is especially challenging to isolate top equilibrium candidates for the wide 1200–1700 K temperature range. As seen in Figs. 3f and 4f, only two alloys have consistently high predicted (S)YS across the full temperature range due to the difficulties of finding candidates that have stable BCC phases across the entire range and that can operate at 1700 K. The identified metastable alloys could be suitable for use durations shorter than the metastability lifetime at a given temperature.

Through comparison of the analytic predictions, it is clear that many candidates, both equilibrium and metastable, are nonetheless predicted to outperform MoNbTaVW and CrMoNbV by considerable margins in terms of our criteria and objectives. The identified metastable alloys have predicted YS values up to 75% higher and SYS values up to 35% higher than CrMoNbV. These prominently feature W and Cr, Cr-W and Nb-W pairs, and the Cr-Nb-W, Nb-W-Zr, and effective Cr-W systems. The identified robustly stable alloys have predicted YS values up to 100% higher and SYS values up to 160% higher than MoNbTaVW. These prominently feature Cr, Hf, Mo, and W, Hf-Mo, Cr-Mo, and Cr-W pairs, and the Hf-Mo-Ta, Mo-Ta-Zr, Cr-Mo-W, and Cr-Mo systems.

About one-third of the alloys identified in Figs. 3 and 4 can be considered binary MPEAs, with <10% of one element. The recommended Hf-Mo-Nb alloys and some of the Hf-Mo-Ta alloys are not MPEAs, with <10% of two elements. These can be considered dilute ternaries. The remaining alloys fit the medium entropy alloy category, with three or four principal components[24].

Comparison of *Part I* and *Part II* alloys

Preliminary alloy recommendations based on general principles and quick down-selection procedures were provided in *Part I* of this series. As the analyses in *Parts I* and *II* were done nearly independently, it is interesting to question if the methods produce similar recommendations for ternary systems.

The following are the key differences between the methods. In *Part II*, the down-selection from 165 to 13 systems was based on metastable YS (with respect to phase separation) only, whereas those in *Part I* were separately down-selected for metastable YS, metastable SYS, equilibrium YS, and equilibrium SYS cases. Ternary systems in *Part II* were required to have a relatively large domain in composition–temperature space with high YS and good phase stability. However, temperature ranges were not considered in *Part I*; high (S)YS and BCC phase stability were required only at one temperature and one composition. Additional constraints were also imposed in *Part II*; an alloy was considered viable only for
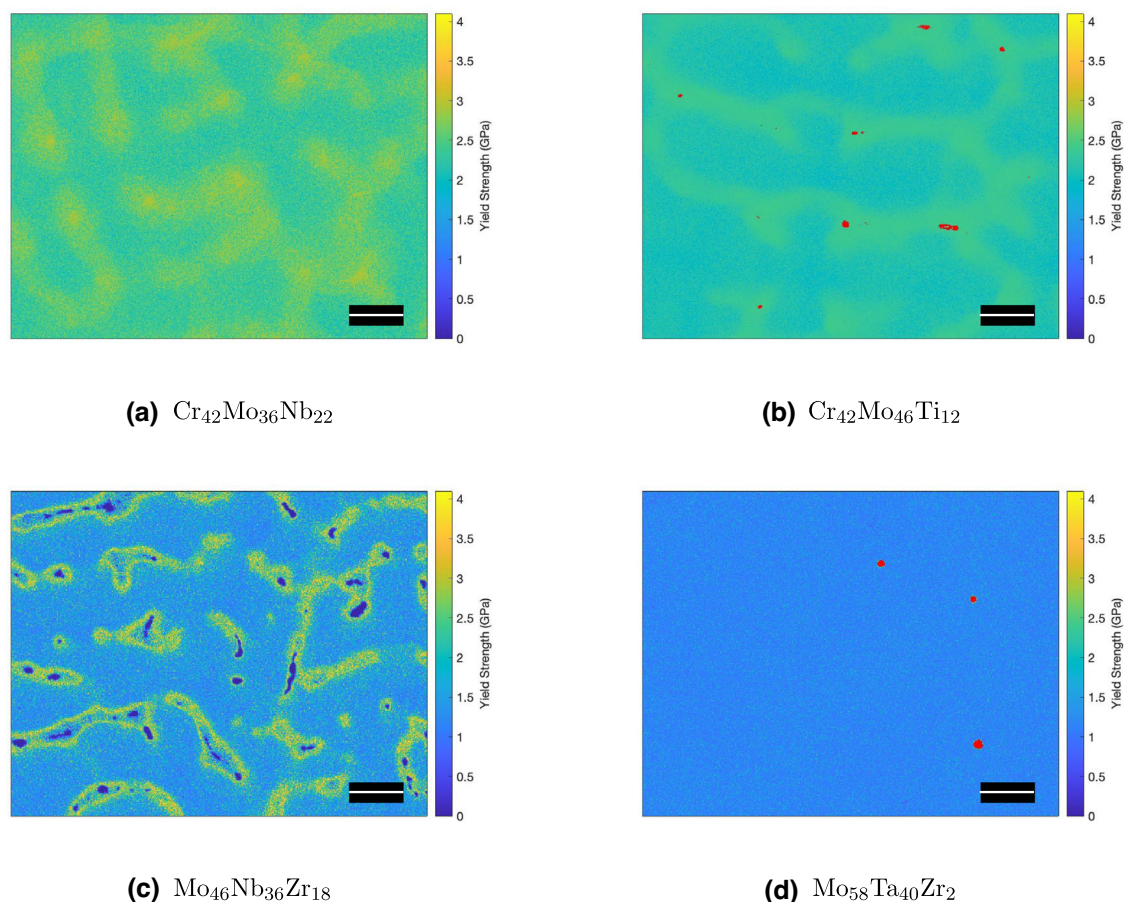
(a) $Cr_{42}Mo_{36}Nb_{22}$

(b) $Cr_{42}Mo_{46}Ti_{12}$

(c) $Mo_{46}Nb_{36}Zr_{18}$

(d) $Mo_{58}Ta_{40}Zr_2$

Fig. 7 Predicted yield strength maps. Predicted yield strength maps from EDS composition measurements for **a** $Cr_{42}Mo_{36}Nb_{22}$, **b** $Cr_{42}Mo_{46}Ti_{12}$, **c** $Mo_{46}Nb_{36}Zr_{18}$, and **d** $Mo_{58}Ta_{40}Zr_2$. The red pixels in (**b**) and (**d**) are regions erroneously rich in Ti and Zr, respectively, which have been left out of the YS prediction, as discussed in the Supplementary Information ("Energy dispersive spectroscopy results" section). Scale bar: 20 μm.

$T \leq 0.6 T_m$ and was required to be at least 4% in composition space away from any non-100% BCC phase boundary for all temperatures being considered. Given these differences, we now assess the resulting magnitude of variations in recommended ternary alloys between methods.

Overall, the top ternary systems identified in *Parts I* and *II* are quite similar, and the reasons for the differences that do exist are clear. Table 2 lists the single top ternary and quaternary systems suitable for comparison between *Parts I* and *II*, and Fig. 5 of *Part I* further displays high-performing ternary systems in equilibrium at 1300 K for YS and SYS. The combined top nine equiatomic and top eight Pareto ternary systems (both sets including metastable candidates) from *Part I* include 11 of the 13 *Part II* ternary down-selects. The two systems from *Part II*'s final 13 that were not identified in *Part I* are Cr-Mo-V and Cr-Ti-W. These did not appear in the equiatomic analysis because they have low equiatomic YS and are not outstanding enough at any composition to appear on the Pareto front. All down-selected Cr-Mo-V compositions in *Part II* are also effectively Cr-Mo binaries, containing 2% V. All down-selected Cr-Ti-W compositions in *Part II* similarly contain relatively low levels of either Ti or Cr.

The four systems from *Part I*'s top nine equiatomic and top eight Pareto ternary systems noted above that are not included in *Part II*'s initial 16 down-selects are Cr-Nb-V, Nb-V-Zr, Cr-Hf-Mo, and Al-Fe-Zr. Cr-Nb-V and Nb-V-Zr were judged slightly too weak and/ or unstable overall to pass the first down-selection in *Part II*. Cr-Hf-Mo and Al-Fe-Zr were cut because each is only stable over a small area with low Hf and Zr contents, respectively.

The Hf-Mo-Ta and Hf-Mo-Nb systems were the best-performing ternaries at 1300 K from both the equiatomic and Pareto analyses in *Part I*. Both of these Hf-containing systems were nearly excluded from *Part II* due to their large irregularly shaped non-BCC domains, as shown in Supplementary Fig. 2c, d in the Supplementary Information. These non-BCC domains likely result from the stable hexagonal close-packed (HCP) phase in Hf at high temperatures. However, based on the results from *Part I*, these candidates were included in the final analysis of *Part II*. Even though only relatively small regions of high YS and BCC phase stability exist in the Hf-Mo-Ta and Hf-Mo-Nb systems, several alloys from these systems were top performers in *Part II*, demonstrating complementary use of the different down-selection methods.

Alloys predicted to have intermetallic phases were excluded from this study as they are known to induce detrimental brittleness. Beyond that consideration, the property of ductility was not addressed, a known issue in refractory BCC MPEAs[9]. Methods based on, e.g., the valence electron concentration[25] and the competition between crack tip growth and dislocation emission mechanisms[26] can be used to predict alloy ductility. Low ductility can also sometimes be mitigated with alternative approaches such as nitrogen doping[27]. In addition, while BCC phase stability between 1200 and 1800 K was carefully considered, the recommended compositions have varying degrees of BCC stability at lower temperatures. Further experimental and computational work is thus needed to confirm the predicted high-temperature strengths of the alloys, examine the appearance of

Table 1. Alloy recommendations: top ternary or binary alloys labeled by the operational temperature range, maximized quantity (yield strength or specific yield strength), and phase stability constraint (metastable with respect to BCC phase separation, equilibrium).

	1200–1500 K	1500–1800 K	1200–1700 K
Yield strength	$Cr_{44}Nb_{16}W_{40}$	$Nb_{30}W_{48}Zr_{22}$	$Cr_{40}Nb_{18}W_{42}$
(Metastable)	$Mo_{44}Ta_{30}Zr_{26}$	$Cr_{36}Nb_{18}W_{46}$	$Nb_{34}W_{38}Zr_{28}$
Yield strength	$Hf_{22}Mo_{38}Ta_{40}$	$Hf_{16}Mo_{52}Ta_{32}$	$Hf_{22}Mo_{38}Ta_{40}$
(Equilibrium)	$Cr_{42}Mo_{46}Ti_{12}$	$Mo_{58}Ta_{32}Zr_{10}$	$Cr_{42}Mo_{26}W_{32}$
Specific yield strength	$Cr_{42}Mo_{36}Nb_{22}$	$Nb_{30}W_{46}Zr_{24}$	$Cr_{40}Nb_{18}W_{42}$
(Metastable)	$Mo_{42}Nb_{30}Zr_{28}$	$Cr_{36}Nb_{18}W_{46}$	$Nb_{34}W_{38}Zr_{28}$
Specific yield strength	$Cr_{40}Mo_{48}Ti_{12}$	$Hf_6Mo_{90}Nb_4$	$Cr_{28}Mo_{50}Nb_{22}$
(Equilibrium)	$Cr_{37}Mo_{63}$	$Mo_{58}Ta_{32}Zr_{10}$	$Cr_{37}Mo_{63}$

The top two alloys with the highest strength are listed for each of the four conditions in the three temperature ranges.

Table 2. Part I and Part II alloys: comparison of top Part II ternaries with top Part I ternaries and quarternaries, as well as experimental reference alloys CrMoNbV[16] (metastable) and MoNbTaVW[8] (equilibrium), all at 1300 K.

Optimization—metastable	Yield strength	Alloy
Part I, 4	2.06	$Al_{20}Fe_{25}W_{50}Zr_5$
Part I, 3	1.87	$Cr_{44}Nb_{20}W_{36}$
Part II, 3 (1300)	1.86	$Cr_{44}Nb_{18}W_{38}$
Part II, 3 (1200–1500)	1.85	$Cr_{44}Nb_{16}W_{40}$
Experiment	1.06	CrMoNbV

Optimization—equilibrium	Yield strength	Alloy
Part I, 4	1.53	$Hf_{25}Mo_{40}Ta_{30}Zr_5$
Part I, 3	1.53	$Hf_{32}Mo_{40}Ta_{28}$
Part II, 3 (1300)	1.46	$Hf_{32}Mo_{38}Ta_{30}$
Part II, 3 (1200–1500)	1.31	$Hf_{22}Mo_{38}Ta_{40}$
Experiment	0.83	MoNbTaVW

Optimization—metastable	Specific yield strength	Alloy
Part I, 4	0.22	$Al_5V_{50}W_{15}Zr_{30}$
Part I, 3	0.19	$Cr_{54}Mo_{26}Nb_{20}$
Part II, 3 (1300)	0.185	$Cr_{54}Mo_{28}Nb_{18}$
Part II, 3 (1200–1500)	0.178	$Cr_{42}Mo_{36}Nb_{22}$
Experiment	0.133	CrMoNbV

Optimization—equilibrium	Specific yield strength	Alloy
Part I, 4	0.17	$Fe_{30}Mo_{10}Ti_{45}Zr_{15}$
Part I, 3	0.19	$Al_{32}Fe_{58}Zr_{10}$
Part II, 3 (1300)	0.158	$Cr_{52}Mo_{34}Ti_{14}$
Part II, 3 (1200–1500)	0.143	$Cr_{40}Mo_{48}Ti_{12}$
Experiment	0.069	MoNbTaVW

Optimizations are labeled by phase stability constraint (metastable with respect to BCC phase separation or equilibrium), Part I or II, and alloy complexity (3 or 4 elements). Part II optimizations are also labeled by temperature or temperature range considered (units are K). Yield strength and specific yield strength units are GPa and GPa cm^3 g^{-1}. CrMoNbV values are extrapolated from 1273 K, and MoNbTaVW values are interpolated between 1273 and 1473 K data.

other phases at lower temperatures, assess the stability of the recommended metastable alloys, and ensure sufficient ductility.

Overall discussion

Parts I and II of this work comprise a relatively wide-ranging and in-depth exploration of design rules and down-selection procedures to identify strong, stable, and lightweight refractory BCC MPEAs, especially ternaries, from the Al-Cr-Fe-Hf-Mo-Nb-Ta-Ti-V-W-Zr family. The work targeted maximization of (S)YS and BCC phase stability at temperatures between 1200 and 1800 K, with specified constraints.

In Part II, the search has been pursued within a more constrained and application-relevant design space than was considered in Part I. A more comprehensive and targeted design approach has been developed and applied to explore all 165 ternary systems in the 11-element family and find high-performing alloys that satisfy multiple constraints in the 1200–1800 K temperature range. Ternary alloys were selected for their tractability and because they were found in Part I to be generally as high-performing or higher-performing than alloys with more elements.

A subset of ternary systems that contain large contiguous areas in composition–temperature space with both high strength and robust BCC phase stability was first delineated. Twelve sets of 5–15 high-performing alloys were then identified, each set optimized for one combination of phase constraint (metastable or equilibrium), optimization target (YS or SYS), and temperature range (1200–1500 K, 1500–1800 K, or 1200–1700 K). Note that alloys designated metastable in this work are metastable only with respect to phase separation into two BCC phases. All compositions predicted to have any non-BCC phases are excluded from consideration. Each identified alloy maximizes (S)YS over a finite temperature range, not only at a single temperature, and is constrained over this temperature range to be 100% BCC (single- or dual-phase) and at least 4% in composition space from any non-BCC phase boundary. Each alloy must also satisfy $T \le 0.6T_m$ to be deemed serviceable at a given temperature.

The identified ternary alloys are thus designed to be more robustly stable and high-performing over specific temperature ranges than those in Part I. These alloys have (S)YS values that are comparable, though generally slightly lower (1–25%), than those of the alloys identified in Part I. This is because simultaneous satisfaction of the added constraints further applied over a range of temperatures, typically requires some sacrifice in strength.

Through comparison of the analytic predictions, it is clear that the identified metastable alloys have predicted YS values up to

75% higher and SYS values up to 35% higher than metastable alloys reported to date. The identified robustly stable alloys have predicted YS values up to 100% higher and SYS values up to 160% higher than stable alloys reported to date. Several of the stable alloys include coexisting BCC phases, an MPEA category that has not been well-explored.

Preliminary room-temperature hardness measurements on 10 down-selected alloys demonstrate qualitative agreement between predictions and experiment and quantitative agreement within 7–17% for eight of the 10 alloys. EDS compositional analyses indicate that the larger discrepancies may be due to secondary phase formation and/or strong microsegregation in the as-cast state. The experimental results thus support the viability of the proposed MPEA design methodology and implementation, though further high-temperature testing is needed to fully verify our predictions.

The three different down-selection procedures applied in Parts I and II produce similar but not identical top ternary systems and somewhat different alloy compositions. The variations are largely traceable to the different regions of composition–temperature

space explored and the different constraints applied. Together the three methods provide complementary insights into the design of refractory MPEAs and verify the robustness of the design principles examined in this work. They have also yielded many candidates with predicted strengths 2–3 times higher than refractory MPEAs reported to date and BCC phase stability.

The findings of *Parts I* and *II* highlight the importance of exploring regions away from the equiatomic center of composition space, applying application-relevant constraints, and systematically incorporating BCC phase stability predictions into the design process to fully account for and optimize over the trend of opposition between strength and phase stability. From this basis, further exploration and design of more complex and tightly constrained MPEA systems can be more effectively pursued.

METHODS

Computational methods

The computational methods used are the same as in *Part I* of this series, as briefly re-summarized here. Phase stability predictions were made using the CALPHAD method based on Thermo-Calc 2021a with the TCHEA4 database and TQ-interface[28]. Thermodynamic quantities over the composition spaces of all 165 ternary systems in the 11-component Al-Cr-Fe-Hf-Mo-Nb-Ta-Ti-V-W-Zr family were computed on regular grids with a composition step size of 2 at.%. For down-selected alloys, quantities at each composition were computed on a regular grid of temperatures from 300 to 3700 K with a step size of 100 K.

The analytic and parameter-free mechanistic YS model of Maresca and Curtin[17,29] describes BCC MPEA solid solution strengthening associated with edge dislocations in terms of elemental atomic volumes and elastic moduli. The YS σ_y is calculated as

$$\sigma_y(T, \dot{\epsilon}) = \begin{cases} \sigma_{y0}\left[1 - \left(\frac{kT}{\Delta E_{b0}}\ln\frac{\dot{\epsilon}_0}{\dot{\epsilon}}\right)^{2/3}\right], \sigma_y/\sigma_{y0} \geq 0.5 \\ \sigma_{y0}\exp\left(-\frac{1}{0.55}\frac{kT}{\Delta E_{b0}}\ln\frac{\dot{\epsilon}_0}{\dot{\epsilon}}\right), \sigma_y/\sigma_{y0} < 0.5 \end{cases} \tag{1}$$

where T is temperature, $\dot{\epsilon}$ is strain rate (set to 10^{-3} s^{-1} in this work), σ_{y0} is the zero-temperature YS, k is Boltzmann's constant, ΔE_{b0} is the zero-stress energy barrier, and $\dot{\epsilon}_0$ is a reference strain rate set to 10^4 s^{-1} from ref. [17]. Complete definitions of σ_{y0} and ΔE_{b0} can be found in *Part I*.

Reference [17] compares this analytic YS model with experimental data from alloys in the Mo-Nb-Ta-V-W family for temperatures up to 1900 K, and the results are in relatively good agreement. One missing feature discussed is the plateau in YS versus temperature seen at high temperatures in experimental data but not in the theory-predicted results. Furthermore, in general, since the model describes strengthening due only to edge dislocations and neglects contributions from screw dislocations and other mechanisms, as discussed in ref. [17], the model may tend to underpredict experimental YS values when valid. Alloys with, e.g., screw-controlled strengthening are likely screened out in this work as their predicted YS should be small. The use of the model in YS optimization is thus self-selecting for refractory MPEAs whose strength is controlled by edge dislocations.

As further validation for this study, several binary, ternary, and quaternary alloys from the Cr-Mo-Nb-V-W family (and MoNbTaVW) were hardness tested at room temperature and compared with model predictions. Results, provided in Supplementary Fig. 7 in the "Yield strength model validation" section of the Supplementary Information, demonstrate trends consistent with the above expectations and good overall quantitative agreement between experiments and predictions.

Experimental methods

The strengths and microstructures of two groups of alloys were assessed experimentally to further validate the Maresca-Curtin YS model[17] and to facilitate the interpretation of experiment–model comparisons.

Sample preparation

For all investigated alloys, buttons produced by vacuum arc melting were sectioned laterally in the middle to obtain $10 \times 10 \times 3$ mm rectangular cuboids. The cuboids were mounted in graphite-based conductive mounting powders and polished down sequentially to 1200 fine grit using silicon carbide papers. The 1200 fine-grit polished samples were further polished with 3 μm and 1 μm diamond suspension before final vibratory polishing in 0.04 μm colloidal silica suspension for 24 h. Samples were triple-washed by sonicating in acetone, isopropyl alcohol, and finally methanol, sequentially for 10 min in each solution.

Microhardness characterization

Microhardness characterization of the various refractory MPEAs was made with the Wilson VH3100 Vickers Microhardness Tester[30]. The indenter used was a Vickers diamond pyramidal indenter at test scales of HV1 (1 kg load) and HV2 (2 kg load). The Vickers hardness (H_V) was calculated automatically by the DiaMet software[31] from the relation:

$$H_V = 0.1891\frac{P}{d^2} \tag{2}$$

where P is the applied load measured in kilogram-force and d is the average of both diagonal indentation impression lengths measured in mm (optically measured by bright field overview camera equipped with ×50 zoom lens). Twenty indents were made at HV1 and HV2, and indents that fell within 15% of two prior indents were accepted, while those above 15% were re-indented to avoid regions that may have microstructural or crystallographic texture. The mean value of the HV1 indents was calculated and reported, while the HV2 indents were primarily inspected for crack formation around the diagonal tips. The elastic recovery of materials upon removal of normal load applied to the indenter is assumed to be negligible as the indentation diagonal lengths are considered. For comparison with the YS predictions, the Vickers hardness is converted to YS (σ_y) in GPa using Tabor's relation, $\sigma_y \approx H_V/300$ from ref. [32]. The validity of this relation for refractory MPEAs is demonstrated in ref. [33].

Microstructure characterization

Energy dispersive spectroscopy (EDS) was used to provide a semi-quantitative analysis of the distribution of elements within a representative area of some alloys. The EDS scans are 512×400 pixels with a pixel size of 300 nm^2. A ThermoFisher Apreo 2 scanning electron microscope (SEM) equipped with an EDAX Octane Elite Super EDS detector was used to collect the EDS spectra under the following beam conditions: a 20 kV accelerating voltage, 0.4 nA beam current, and 10 mm working distance. The scans had a dwell time of 200 μs per pixel per frame over 64 frames with an average signal of 3.6×10^4 to 4×10^4 counts per second. EDAX APEX software was used to perform a ZAF analysis on the area scans to produce a composition value for each pixel in atomic percent.

DATA AVAILABILITY

The data supporting the findings of this study are available within the paper and its supplementary files and are available from the corresponding author upon reasonable request.

CODE AVAILABILITY

The codes used during the current study are available from the corresponding author upon reasonable request.

REFERENCES

1. Miracle, D. B. & Senkov, O. N. A critical review of high entropy alloys and related concepts. *Acta Mater.* **122**, 448–511 (2017).
2. Senkov, O. N., Gorsse, S. & Miracle, D. B. High temperature strength of refractory complex concentrated alloys. *Acta Mater.* **175**, 394–405 (2019).
3. Savage, N. High-entropy alloys expand their range. *Nature* **595**, S4–S5 (2021).
4. Yeh, J. et al. Nanostructured high-entropy alloys with multiple principal elements: novel alloy design concepts and outcomes. *Adv. Eng. Mater.* **6**, 299–303 (2004).
5. Cantor, B., Chang, I. T. H., Knight, P. & Vincent, A. J. B. Microstructural development in equiotomic multicomponent alloys. *Mater. Sci. Eng. A* **375-377**, 213–218 (2004).
6. Praveen, S. & Kim, H. S. High-entropy alloys: potential candidates for high-temperature applications—an overview. *Adv. Eng. Mater.* **2018**, 1700645 (2017).
7. Kang, B., Kong, T., Ryu, H. J. & Hong, S. H. Superior mechanical properties and strengthening mechanisms of lightweight AlxCrNbVMo refractory high-entropy alloys (x=0,0.5,1.0) fabricated by the power metallurgy process. *J. Mater. Sci. Technol.* **69**, 32–41 (2021).
8. Senkov, O. N., Wilks, G. B., Scott, J. M. & Miracle, D. B. Mechanical properties of $Nb_{25}Mo_{25}Ta_{25}W_{25}$ and $V_{20}Nb_{20}Mo_{20}Ta_{20}W_{20}$ refractory high entropy alloys. *Intermetallics* **19**, 698–706 (2011).
9. Srikanth, M., Annamalai, A. R., Muthuchamy, A. & Jen, C. A review of the latest developments in the field of refractory high-entropy alloys. *Crystals* **11**, 612 (2021).
10. Zhang, Y. et al. Microstructures and properties of high entropy alloys. *Prog. Mater. Sci.* **61**, 1–93 (2014).
11. Yeh, J. Recent progress in high entropy alloys. *Ann. Chim.: Sci. Mater.* **31**, 633–648 (2006).
12. Zhang, Y., Yang, X. & Liaw, P. K. Alloy design and properties optimization of high entropy-alloys. *JOM* **64**, 830–838 (2012).
13. Knabl, W., Leichtfried, G. & Stickler, R. *Springer Handbook of Materials Data* (Springer, 2018).
14. Senkov, O. N., Wilks, G. B., Miracle, D. B., Chuang, C. P. & Liaw, P. K. Refractory high-entropy alloys. *Intermetallics* **18**, 1758–1765 (2010).
15. Tseng, K.-K. et al. Effects of Mo, Nb, Ta, Ti, and Zr on mechanical properties of equiatomic Hf-Mo-Nb-Ta-Ti-Zr alloys. *Entropy* **21**, 15 (2018).
16. Feng, R. et al. Superior high-temperature strength in a supersaturated refractory high-entropy alloy. *Adv. Mater.* **33**, 2102401 (2021).
17. Maresca, F. & Curtin, W. A. Mechanistic origin of high strength in refractory BCC high entropy alloys up to 1900 K. *Acta Mater.* **182**, 235–249 (2020).
18. Lukas, H., Fries, S. G. & Sundman, B. *Computational Thermodynamics: The Calphad Method* (Cambridge University Press, 2007).
19. Spencer, P. J. A brief history of CALPHAD. *Calphad* **32**, 1–8 (2008).
20. Borg, C. K. H. et al. Expanded dataset of mechanical properties and observed phases of multi-principal element alloys. *Sci. Data* **7**, 430 (2020).
21. Basu, I. & De Hosson, J. T. M. Strengthening mechanisms in high entropy alloys: fundamental issues. *Scr. Mater.* **187**, 148–156 (2020).
22. Smallman, R. E. & Ngan, A. H. W. *Modern Physical Metallurgy* (Oxford, 2014).
23. Kube, S. A. & Schroers, J. Metastability in high entropy alloys. *Scr. Mater.* **186**, 392–400 (2020).
24. Cao, F., Munroe, P., Zhou, Z. & Xie, Z. Medium entropy alloy CoCrNi coatings: enhancing hardness and damage-tolerance through a nanotwinned structuring. *Surf. Coat. Technol.* **335**, 257–264 (2018).
25. Chen, R. et al. Composition design of high entropy alloys using the valence electron concentration to balance. *Acta Mater.* **144**, 129–137 (2018).
26. Mak, E., Yin, B. & Curtin, W. A. A ductility criterion for BCC high entropy alloys. *J. Mech. Phys. Solids* **152**, 104389 (2021).
27. Wang, R. et al. Achieving high strength and ductility in nitrogen-doped refractory high-entropy alloys. *Mater. Des.* **213**, 110356 (2022).
28. Andersson, J.-O., Helander, T., Höglund, L., Shi, P. & Sundman, B. Thermo-Calc & DICTRA, computational tools for materials science. *Calphad* **26**, 273–312 (2002).
29. Lee, C. et al. Strength can be controlled by edge dislocations in refractory high-entropy alloys. *Nat. Commun.* **12**, 5474 (2021).
30. Wilson VH3100 Vickers and Knopp Hardness Testers. https://www.buehler.com/products/hardness-testing/vickers-knoop-hardness-testers/wilson-vh3100-vickers-knoop-hardness-testers/ (Buehler, 2022).
31. DiaMet Hardness Testing Software https://www.buehler.com/products/hardness-testing/automation-software/diamet-hardness-testing-software/ (Buehler, 2022).
32. Tabor, D. A simple theory of static and dynamic hardness. *Proc. R. Soc. A: Math. Phys. Eng. Sci.* **192**, 247–274 (1948).
33. Yao, H. W., Qiao, J. W., Hawk, H. F., Chen, M. W. & Gao, M. C. Mechanical properties of refractory high-entropy alloys: experiments and modeling. *J. Alloys Compd.* **696**, 1139–1150 (2017).

AUTHOR CONTRIBUTIONS

K.L.M.E.: Conceptualization (supporting); Data curation—theory (lead); Formal analysis (lead); Investigation—theory (equal); Methodology (lead); Software (lead); Validation (lead); Visualization (lead); Writing/original draft preparation (lead). J.B.: Conceptualization (lead); Funding acquisition (supporting); Methodology (supporting); Software (supporting); Supervision—theory (lead); Validation (supporting); Writing/original draft preparation (supporting). A.P.: Funding acquisition (supporting); Investigation—theory (equal); Methodology (supporting); Supervision—theory (supporting). B.B.: Investigation—theory (supporting). J.S.: Investigation—experiment (equal); Resources—experiment (lead). C.J.R.: Investigation—experiment (equal). H.B.H.: Supervision—experiment (equal). S.K.M.: Funding acquisition (supporting); Project administration (equal); Supervision—experiment (equal). J.T.M.: Funding acquisition (lead); Project administration (equal); Supervision—experiment (equal).

COMPETING INTERESTS

The authors declare no competing interests.

ADDITIONAL INFORMATION

Supplementary information The online version contains supplementary material available at https://doi.org/10.1038/s41524-023-01031-6.

Correspondence and requests for materials should be addressed to Kate L. M. Elder.

Reprints and permission information is available at http://www.nature.com/reprints

Publisher's note Springer Nature remains neutral with regard to jurisdictional claims in published maps and institutional affiliations.